Realistic Simulation of Local Image Appearance of Cardiac Magnetic Resonance Imaging Using a Virtual Phantom Population

Catalina Tobon-Gomez, Federico Sukno, Bart H. Bijnens, Marina Huguet, Alejandro Frangi

HAL Id: inria-00417839
https://inria.hal.science/inria-00417839

Submitted on 17 Sep 2009

Realistic Simulation of Local Image Appearance of Cardiac Magnetic Resonance Imaging Using a Virtual Phantom Population

C. Tobon-Gomez[1,2,4], F. Sukno[2,1], B. H. Bijnens[3,1,2], M. Huguet[4,2], and
A. F. Frangi[1,2]

[1] Center for Computational Imaging & Simulation Technologies in Biomedicine
(CISTIB), Universitat Pompeu Fabra (UPF),
[2] Networking Biomedical Research Center on Bioengineering, Biomaterials and
Nanomedicine (CIBER-BBN),
[3] Instituciò Catalana de Recerca i Estudis Avançats (ICREA), Barcelona, Spain.
[4] CETIR Sant Jordi, Barcelona, Spain. *

Abstract. Magnetic resonance imaging (MRI) simulators have been largely applied to brain studies. However, cardiac applications of these simulators are only emerging. This paper focuses on the realistic simulation of local appearance of cardiac MRI datasets. Simulations are obtained from the MRISIM simulator with XCAT phantom (formerly NCAT) as input. Phantoms are further extended to increase realism of the local appearance of the simulated datasets. The extension is based on: resemblance of partial volume effect by using a higher resolution phantom as input to the simulator, addition of intensity variability of each tissue by increasing the number of labels of the phantom, and inclusion of trabeculae in the ventricular cavities. The clinical database included 40 patients for anatomical measurements and 5 healthy athletes for local grey value statistics. The virtual database included 20 digital phantoms. Histograms from different tissues were obtained from the real datasets and compared to histograms of the simulated datasets by means of *Chi-square* dissimilarity metric. The addition of sublabels and trabeculae improved the matching of real histograms in 8 out of 11 comparisons. Simulated intensity distributions were improved up to 76% with respect to the original distributions. Our methodology obtained a higher dissimilarity metric for lung and pericardial tissue.

1   Introduction

In spite of the high technological developments in medical imaging systems, cardiac function is still mostly analyzed through visual assessment. This has generated the need for automated processing algorithms to support diagnosis. An interesting way to develop these algorithms is by using simulated datasets,

Table 1. Anatomical parameters for torso and heart variation according to gender

Gender	TORSO							HEART							
	Torso		Ribcage		Breasts			Size*		Orient*		Trans*		Peric*	Trab
	LA	SA	LA	SA	LA	SA	θ	Lth	Diam	ϕ	ψ	Lat	P-A	Thck	Lth
	cm	cm	cm	cm	cm	cm	°	cm		°	°	cm	cm	cm	mm
Female Mean	31.4	21.3	26.0	18.1	18.2	4.8	141	7.2	4.6	27	40	5.2	-5.0	1.2	4.29
SD	2.99	2.44	2.13	2.24	2.32	1.5	2	0.5	0.3	9	13	1.1	2.6	0.8	1.02
Max	35.1	24.9	28.9	22.2	21.0	8.4	176	8.1	5.1	54	76	8.5	0.2	2.5	6.25
Min	23.8	15.0	20.7	12.5	11.5	2.0	110	6.3	4.1	8	16	3.0	-10.6	0.0	1.56
Male Mean	34.6	25.2	29.8	21.5	*n.a.*	*n.a.*	*n.a.*	8.3	5.0	21	36	5.6	-6.4	1.2	4.29
SD	2.12	2.37	2.12	2.77	*n.a.*	*n.a.*	*n.a.*	0.6	0.4	9	12	1.1	2.6	0.8	1.02
Max	37.7	30.3	34.4	27.0	*n.a.*	*n.a.*	*n.a.*	9.4	5.8	41	73	8.0	1.2	2.5	6.25
Min	28.5	20.4	25.4	17.1	*n.a.*	*n.a.*	*n.a.*	7.0	4.2	0	15	3.5	-11.6	0.0	1.56

* Parameters from [7], [8] and [9]; Orient= Orientation; Trans= Translation; Peric= Pericardium;
Trab= Trabeculae; Lth=Length; Diam= Diameter; Thck= Thickness; LA= Long Axis;
SA= Short Axis; Lat= Lateral; P-A= Posterior-anterior; *n.a.*= Not applicable.

which has several advantages. Firstly, large databases can be generated with either normal cases or extreme anatomical variants. Secondly, algorithms can be updated to account for the rapid evolution of imaging technologies, for instance: *i)* improvement of spatial resolution, *ii)* increase of temporal resolution, *iii)* better reconstruction techniques, *iv)* isotropic voxels, *v)* variation on acquisition parameters, etc. Finally, since image simulators of every major modality are currently available [1–3], the collection of a consistent multimodal database is improved.

Magnetic resonance imaging (MRI) simulators have been largely applied to brain studies [3, 4]. However, cardiac applications of these simulators are only emerging [5, 6], despite being potentially useful for evaluating image processing algorithms, including segmentation or multimodal registration. Simulators usually require as input a virtual phantom in order to compute the desired image. Available digital phantoms are mainly focused on low contrast imaging modalities (i.e. nuclear medicine) where a macroscopic representation of the tissues is suitable. However, a modality like MRI requires greater detail to represent the different components of each body tissue. This paper focuses on the realistic simulation of local appearance of cardiac MRI datasets. Our methodology is based on the XCAT phantom (formerly NCAT) [2]. Phantoms are further extended to increase realism of the simulated datasets. The extension is based on: resemblance of partial volume effect by using a higher resolution phantom as input to the simulator, addition of intensity variability of each tissue by increasing the number of labels of the phantom, and inclusion of trabeculae in the ventricular cavities (see Section 3.2 for details).

2   Materials

MRI studies were acquired using a General Electric Signa CVi-HDx, 1.5T scanner (General Electric, Milwaukee, USA). Images were scanned with a balanced

Steady State Free Precession (bSSFP) sequence. The resolution was 1.56mm × 1.56mm × 8mm.

The clinical database included two subgroups:

- *G1:* a group of 40 patients, consisting of axial slices. Variability of anatomical geometry was characterized from this group. Measurements of torso, ribcage, breast and trabeculae dimensions were collected, allowing us to obtain $mean \pm SD$ values. Results are displayed on Table 1.
- *G2*: a group of 5 patients, composed of short-axis stacks, to be compared with the simulated images. This group consisted exclusively of healthy athletes whose scans are often of higher quality than those acquired from an average patient. Also, the absence of subcutaneous fat in these subjects results in intensity distributions with less noise and dispersion.

3   Methods

3.1   Image Formation

MRI Simulator: the MRI simulation code used in this work was developed by Kwan *et al.* [3]. The code models the physical phenomena by solving the Bloch equations [10]. Sequence parameters for the simulation were consistent with those of the clinical datasets: pixel size=1.5625 mm, slice thickness=7.8125 mm, slice separation= 0 mm, field of view= 400×400 mm, number of signal averages=1, scan matrix size=256, pulse sequence=CEFAST, TR/TE=2.9/1.2 ms, flip angle=45°. Coil settings created a chemical shift of up to 2 pixels and noise levels of 3%.

3.2   Digital Voxel Phantoms

Original Phantom: a total of 20 virtual subjects were generated with XCAT. Phantoms included relevant thoracic structures, at half expiration, and cardiac structures, at full relaxation (End Diastole). A realistic representation of a clinical population was accomplished by modifying anatomical parameters according to the measured values from dataset *G1*. Each phantom included 8 types of tissue and a background, labeled as displayed in Table 2.

Each phantom consisted of axial slices of 512×512 pixels with an isotropic voxel of 0.78125 mm^3. The isotropy of the volume allowed us to obtain smooth 2D stacks after short-axis reformatting. The number of short-axis slices varied according to the length of the left ventricle (LV) ensuring the complete inclusion of all cavities. Axial stacks were reformatted to short-axis with the true rotation angles used during phantom generation. Each simulated MRI slice will then contain 10 slices of the input phantom (slice thickness=7.8125 mm/phantom thickness=0.78125 mm).

Table 2. Tissue Magnetic Parameters.

Label		0	1	2	3	4	5	6	7	8
Sublabel		0-27	28-55	56-83	84-111	112-139	140-167	168-195	196-223	224-251
Tissue		Bkg	Lung	Bone	Body	Liver	Gastric	Peric	Myo	Blood
PD	Mean	0	0.07	0.08	0.25	0.45	0.71	1.00	0.60	0.90
	SD	0	0.10	0.01	0.20	0.15	0.25	0.50	0.02	0.30
	Max	0	0.15	0.10	0.30	0.50	0.90	1.00	0.64	1.00
	Min	0	0.00	0.00	0.24	0.40	0.62	0.50	0.54	0.85
	Mean	0	1199	269	549	586	765	500	982	1516
	SD	0	117	30	52	39	75	37	46	21
T1	Max	0	1380	329	653	664	915	574	1092	1558
	Min	0	1040	209	445	508	615	426	902	1474
	Mean	0	79	55	49	46	58	115	54	224
	SD	0	29	21	20	20	24	21	4	26
T2	Max	0	137	97	89	86	106	157	45	276
	Min	0	21	13	9	6	10	73	62	172
	Mean	0	30	35	16	27	30	68	33	199
	SD	0	4	3.8	4	6	4	8	8	8
T2*	Max	0	38	43	24	38	34	77	49	215
	Min	0	22	27.6	8	17	26	45	16	183

Bkg= Background; Peric= Pericardium; Myo= Myocardium

Parameters selected from the review of [6, 11–21]

Extended Phantom: phantoms were further extended to increase realism of the simulated datasets. Our strategy is based on three concepts:

- *Partial volume effect:* aiming to resemble the partial volume effect observed at the edges of most organs, a higher resolution phantom was used as input to the simulator (double the in-plane resolution). Therefore, the intensity value of each voxel in the output image included the contribution of 40 voxels from the input phantom: 4 pixels in each of the 10 slices (see Fig. 1 (a) and (b)).

- *Tissue sublabels:* in order to increment intensity variability for each tissue, the number of labels in the input phantom was increased. Each phantom was modified such that each original tissue label included 27 randomly distributed sublabels (reaching the 255 maximum labels allowed by the simulator). Each sublabel was assigned its corresponding magnetic properties, depending on its original tissue class. The properties for each new sublabel was sampled from a normal distribution with the $mean \pm SD$ values listed in Table 2.

- *Trabeculae inclusion:* in MRI datasets, the region near the myocardial boundary usually appear to have a lighter intensity signal. This is due to the combined contribution of blood and endocardial trabecular structures. The amount of ventricular trabeculae increases from base to apex. They are absent along the outflow track towards the aorta in the LV and towards the pulmonary trunk in the right ventricle (RV) [22]. Finally, trabeculae are
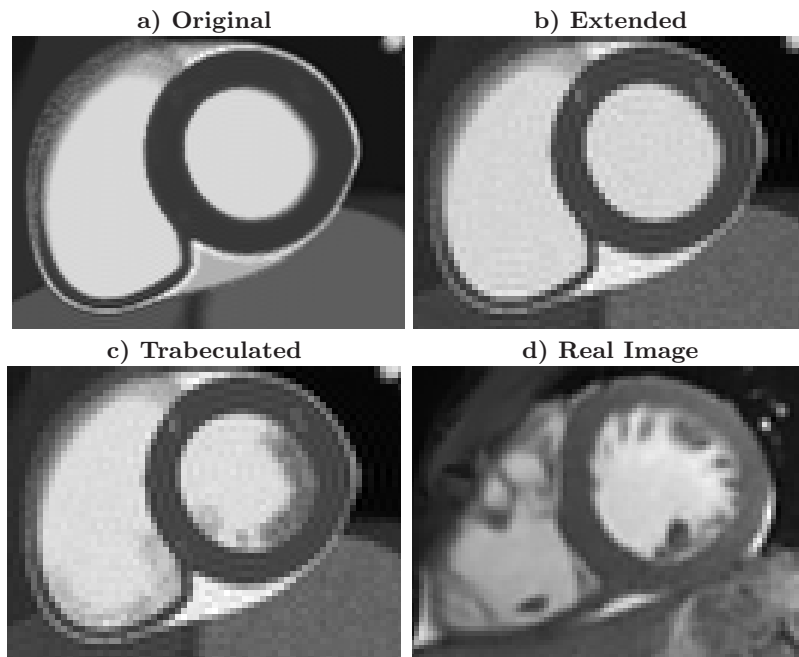
Fig. 1. (a-c) Simulation results with the every type of input phantom. (d) Example of a real image.

more visible in End Diastole (ED) and seem to disappear towards End Systole (ES) as they become part of the wall.

Their presence was simulated by randomly assigning myocardium labels to the inner region along the walls of both ventricles. This region was set to match the thickness of the LV wall. The locations of the trabeculae were selected in two steps: 1) assigning the location of a seed with the functions named below. 2) each seed was replaced with a line structure of different length and directions. The lengths were sampled from the trabecular length values in Table 1. The direction was randomly assigned from 0°to 360°. The density of myocardium of the initial seeds was defined as the multiplication of three functions: *i) $f(distAorta)$*: the radial distance from the aorta, *ii) $f(distLongitudinal)$*: the longitudinal distance from the base and *iii) $f(CycleFrame)$*: the instant of the cardiac cycle (see Fig 2). Trabeculae are predominant on the apical third of both ventricles where they are uniformly distributed along the walls. Therefore $f(distAorta)$ was set to 0.33 for the apical slices.
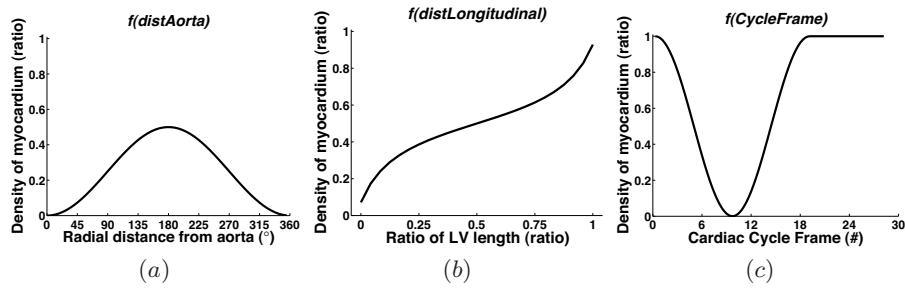
Fig. 2. Underlying functions for the generation of trabeculae: (a) $f(distAorta)$, where *Aorta position* $= 0°$, (b) $f(distLongitudinal)$, where *LV ratio = (distance from base)/(total LV length)*, and (c) $f(CycleFrame)$, where $ED = frame\#1$ and $ES = frame\#10$.

3.3 Experimental Setup

In order to evaluate the realism of simulated results, typical intensity values were obtained from clinical datasets. Intensity values of all samples were normalized in an automatic manner. The minimum of the intensity range was set at the 30th percentile, the maximum was set at the 99.95th percentile. This lower limit corresponds to intensity of the background in real images. The upper limit was set to eliminate high intensity noise.

A region-of-interest (ROI) for each tissue was manually delineated by a researcher experienced in cardiac MRI. Each ROI included the largest possible area with an homogeneous visual appearance. Intensity values inside each ROI were analyzed by means of histograms. The required number of bins was estimated according to Scott's rule (70 bins) [23]. Histograms were calculated automatically from the virtual datasets using the original labeled phantoms. Three comparisons were performed: *i) real vs. original:* real histograms were compared to the simulation-based histograms with the original phantom as input, *ii) real vs. extended:* real histograms were compared to the simulation-based histograms with the extended phantom as input, *iii) real vs. trabeculated:* real histograms were compared to the simulation-based histograms with the trabeculated phantom as input.

Real(**P**) and simulation-based (**Q**) histograms were compared using the *Chi-square* dissimilarity metric [23]:

$$\chi^{\mathbf{2}} = \sum_{i=1}^{n} \frac{(\mathbf{P}_i - \mathbf{Q}_i)^2}{\mathbf{P}_i + \mathbf{Q}_i} \quad \text{where } n \text{ is the number of bins} \tag{1}$$
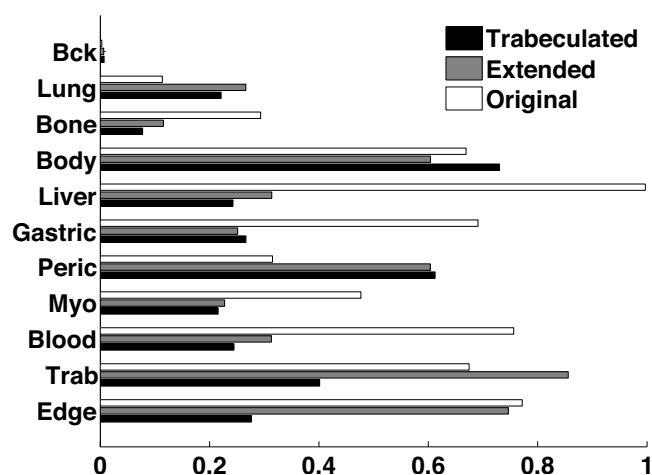
Fig. 3. Bar plot of the *Chi-square* dissimilarity metric for every type of input phantom. Note that lower metric values represent more similar histograms. Bkg= Background; Peric= Pericardium; Myo= Myocardium; Trab= Region of trabeculae, Edge= LV region over the edge.

4 Results

The simulated images using the trabeculated phantom have a more realistic visual appearance compared to those based on the original and the extended phantoms (see Fig. 1).

The result of the *Chi-square* dissimilarity metric evaluation is displayed in Fig. 3. The evaluation was made for each tissue plus the region of trabeculae and a region over the edge of the LV wall (including trabeculae, edge and myocardium). The addition of sublabels and trabecula improved the matching with the real histograms in 8 out of 11 comparisons. The improvement reached 68% for the extended phantom and 76% for the trabeculated phantom.

The four histograms with more relevance for cardiac applications (myocardium, blood, trabeculae and edge) obtained a lower dissimilarity metric in the trabeculated phantom, with respect to the original and extended phantom. However, our methodology obtained a higher dissimilarity metric for lung and pericardial tissue. Real histograms show that lung tissue has less intensity variation than the rest of the tissues, which is probably best modeled with a unique phantom label. The pericardium, due to its mixed composition of fluid and fat, presents a challenge for simulation. Its histogram displayed a sharp peak in the brightest pixels and isolated peaks in the mid-range pixels.

5 Conclusion and Future Work

In this work, we presented a cardiac MRI simulation pipeline based on the MRISIM simulator and XCAT phantoms. These phantoms were extended in order to improve tissue appearance. Performance was measured by comparing data of 20 virtual datasets with 5 high quality clinical datasets. Simulated intensity distributions were improved up to 76% with respect to the original distributions. In this sense, the comparison of histograms indicated a good match between the local image appearance of real and simulated images, with particular improvement on the myocardial wall boundary. Results are quite encouraging for potential use in training model-based segmentation algorithms. Further improvements could involve the incorporation of papillary muscles.

References

1. Ljungberg, M., Strand, S.E.: A monte carlo program simulating scintillation camera imaging. Comp Meth Progr Biomed **29** (1989) 257–272
2. Segars, W.P., Mahesh, M., Beck, T.J., Frey, E.C., Tsui, B.M.: Realistic CT simulation using the 4D XCAT phantom. Med Phys **35**(8) (Aug 2008) 3800–3008
3. Kwan, R.K.S., Evans, A.C., Pike, G.: MRI simulation-based evaluation of image-processing and classification methods. IEEE Trans Med Imaging **18**(11) (1999) 1085–1097
4. Aubert-Broche, B., Evans, A.C., Collins, L.: A new improved version of the realistic digital brain phantom. Neuroimage **32**(1) (Aug 2006) 138–145
5. Anderson, D.J., Dendy, J.M., Paschal, C.B.: Simulation study of susceptibility gradients leading to focal myocardial signal loss. J Magn Reson Imaging **28**(6) (2008) 1402–1408
6. Haddad, R., Magnin, I.E., Clarysse, P.: A new fully-digital anthropomorphic and dynamic thorax/heart model. Engineering in Medicine and Biology Society, 2007. EMBS 2007. 29th Annual International Conference of the IEEE (Aug. 2007) 5999–6002
7. Salton, C.J., Chuang, M.L., O'Donnell, C.J., Kupka, M.J., Larson, M.G., Kissinger, K.V., Edelman, R.R., Levy, D., Manning, W.J.: Gender differences and normal left ventricular anatomy in an adult population free of hypertension. a cardiovascular magnetic resonance study of the framingham heart study offspring cohort. J Am Coll Cardiol **39**(6) (Mar 2002) 1055–1060
8. He, X., Frey, E.C., Links, J.M., Gilland, K.L., Segars, W.P., Tsui, B.M.W.: A mathematical observer study for the evaluation and optimization of compensation methods for myocardial SPECT using a phantom population that realistically models patient variability. IEEE Trans Nucl Sci **51**(1) (Feb 2004) 218–224
9. Ling, L.H., Oh, J.K., Tei, C., Click, R.L., Breen, J.F., Seward, J.B., Tajik, A.J.: Pericardial thickness measured with transesophageal echocardiography: feasibility and potential clinical usefulness. J Am Coll Cardiol **29**(6) (May 1997) 1317–1323
10. Bloch, F.: Nuclear induction. Phys. Rev. **70**(7-8) (Oct 1946) 460–474
11. Bottomley, P.A., Foster, T.H., Argersinger, R.E., Pfeifer, L.M.: A review of normal tissue hydrogen NMR relaxation times and relaxation mechanisms from 1-100 MHz: dependence on tissue type, nmr frequency, temperature, species, excision, and age. Med Phys **11**(4) (1984) 425–448

12. Messroghli, D.R., Plein, S., Higgins, D.M., Walters, K., Jones, T.R., Ridgway, J.P., Sivananthan, M.U.: Human myocardium: single-breath-hold MR T1 mapping with high spatial resolution–reproducibility study. Radiology **238**(3) (Mar 2006) 1004–1012

13. Wacker, C.M., Bock, M., Hartlep, A.W., Beck, G., van Kaick, G., Ertl, G., Bauer, W.R., Schad, L.R.: Changes in myocardial oxygenation and perfusion under pharmacological stress with dipyridamole: Assessment using T1 and T2* measurements. Magnetic Resonance in Medicine **41** (1999) 686–695

14. de Bazelaire, C.M.J., Duhamel, G.D., Rofsky, N.M., Alsop, D.C.: MR imaging relaxation times of abdominal and pelvic tissues measured in vivo at 3.0 T: preliminary results. Radiology **230**(3) (Mar 2004) 652–659

15. Akber, S.F.: An association between spin-lattice relaxation time and organ weight in humans. Med Hypotheses **48**(2) (Feb 1997) 189–191

16. Brix, G., Schad, L.R., Lorenz, W.J.: Evaluation of proton density by magnetic resonance imaging: phantom experiments and analysis of multiple component proton transverse relaxation. Phys Med Biol **35**(1) (Jan 1990) 53–66

17. Huang, T.Y., Liu, Y.J., Stemmer, A., Poncelet, B.P.: T2 measurement of the human myocardium using a T2-prepared transient-state TrueFISP sequence. Magn Reson Med **57**(5) (May 2007) 960–966

18. Wright, G.A., Hu, B.S., Macovski, A.: Estimating oxygen saturation of blood in vivo with MR imaging at 1.5 T. J Magn Reson Imaging **1**(3) (1991) 275–283

19. Westwood, M., Anderson, L.J., Firmin, D.N., Gatehouse, P.D., Charrier, C.C., Wonke, B., Pennell, D.J.: A single breath-hold multiecho T2* cardiovascular magnetic resonance technique for diagnosis of myocardial iron overload. J Magn Reson Imaging **18**(1) (Jul 2003) 33–39

20. Li, D., Wang, Y., Waight, D.J.: Blood oxygen saturation assessment in vivo using T2* estimation. Magn Reson Med **39**(5) (May 1998) 685–690

21. Stadler, A., Jakob, P.M., Griswold, M., Barth, M., Bankier, A.A.: T1 mapping of the entire lung parenchyma: Influence of the respiratory phase in healthy individuals. J Magn Reson Imaging **21**(6) (Jun 2005) 759–764

22. Wilcox, B.R., Cook, A.C., Anderson, R.H.: Anatomy of the cardiac chambers. In: Surgical Anatomy of the Heart. 3rd edn. Cambridge University Press (2004) 11–44

23. Brunelli, R., Mich, O.: Histograms analysis for image retrieval. Pattern Recognition **34**(8) (August 2001) 1625–1637